Microfluidics with ultrasound-driven bubbles

By P. MARMOTTANT[1]†, J. P. RAVEN[1]†, H. GARDENIERS[2],
J. G. BOMER[2] AND S. HILGENFELDT[1]‡

[1]Department of Science and Technology, University of Twente, P.O. Box 217, 7500AE Enschede,
The Netherlands

[2]MESA$^+$ Research Institute, University of Twente, P.O. Box 217, 7500AE Enschede, The Netherlands

Microstreaming from oscillating bubbles is known to induce vigorous vortex flow. Here we show how to harness the power of bubble streaming in an experiment to achieve directed transport flow of high velocity, allowing design and manufacture of microfluidic MEMS devices. By combining oscillating bubbles with solid protrusions positioned on a patterned substrate, solid beads and lipid vesicles are guided in desired directions without microchannels. Simultaneously, the flow exerts controlled localized forces capable of opening and reclosing lipid membranes.

1. Introduction

Driving liquid flow on the micrometer scale in micro-electromechanical systems (MEMS) is of prime importance for, among others, lab-on-a-chip and micromixing applications (see Kopp, de Mello & Manz 1998; Beebe *et al.* 2000; Stroock *et al.* 2002; Thorsen, Maerkl & Quake 2002; Solomon & Mezić 2003). A variety of driving forces is available (see Stone & Kim 2001), typically forcing the liquid through microchannels. Recently, it was shown that the oscillations of microbubbles exposed to ultrasound efficiently induce flow on small scales (see Marmottant & Hilgenfeldt 2003). The leading-order periodic component of this flow cannot be readily used for fluid transport. However, viscous forces at the boundary of the bubble together with the nonlinearity of the Navier–Stokes equations lead to a second-order (in the driving amplitude) flow which is steady, called *acoustic streaming*.

The amplitude of streaming velocities results from a balance between nonlinear driving effects and viscous dissipation. The leading-order oscillatory flow $\boldsymbol{u}_1(t)$, of amplitude u_1 and angular frequency $\omega = 2\pi f$, induces a secondary steady streaming flow $\boldsymbol{u}_s$, driven by the nonlinear inertial forcing $\boldsymbol{f}_s = -\rho\langle\boldsymbol{u}_1\cdot\nabla\boldsymbol{u}_1\rangle$ obtained after averaging the Navier–Stokes equation, of amplitude $f_s \sim \rho u_1^2/\ell$, where ℓ is the length scale of the gradient of u_1 (Nyborg 1958; Lighthill 1978). Along the boundary of an object, viscous attenuation is concentrated in the Stokes oscillatory boundary layer of size $\delta \sim (\eta/\rho\omega)^{1/2}$, with η the viscosity and ρ the density. In this boundary layer the steady streaming force is compensated by viscous forces $\boldsymbol{f}_v = \eta\nabla^2\boldsymbol{u}_s$, of amplitude $f_v \sim \eta u_s/\delta^2 \sim \rho\omega u_s$ (see Squires & Quake 2005). The typical velocity scale of the streaming is therefore $u_s = u_1^2/\omega\ell$ near a boundary.

---

† Present address: Laboratoire de Spectrométrie Physique, CNRS-Université Joseph Fourier, BP 87, F-38047 Saint Martin d'Hères, France.
‡ Present address: Engineering Sciences & Applied Mathematics and Dept. of Mechanical Engineering, Northwestern University, 2145 Sheridan Road, Evanston, IL 60208, USA.
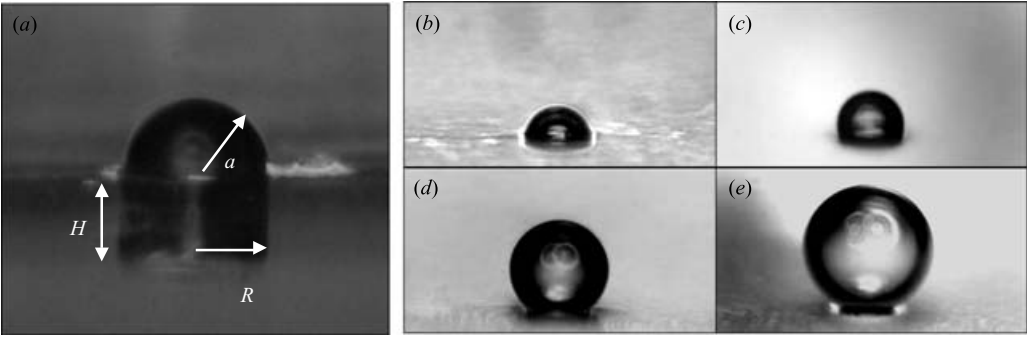
FIGURE 1. Bubbles in isolated pits on a PDMS substrate, in slightly oversaturated water. (*a*) Side view showing the cylindrical pit below the surface of the transparent substrate. Almost-hemispherical bubbles like the one shown here can be stabilized given the right degree of oversaturation (see text). (*b–e*) Time series at higher oversaturation: just after the filling of the cuvette (*b*), after 10 minutes (*c*), 1 hour (*d*) and 3.5 hours (*e*). Pit radius is $R = 60\,\mu$m, pit height $H = 20\,\mu$m.

In our experiments, bubbles (of typical radii $a \sim 10$–$50\,\mu$m) are the source of oscil-latory flow. They are attached to the wall of a small cuvette, in which a piezoelectric transducer generates a standing ultrasound field on length scales $\gg a$ (wavelengths are $\gtrsim 1$ cm). The oscillation amplitude A of the bubble wall is always small, so that $\epsilon \equiv A/a \ll 1$. The streamlines of the steady streaming flow then take the shape of a recirculation vortex torus above the wall and around the bubble, see Marmottant & Hilgenfeldt (2003) and detailed calculation in Hansen, Marmottant & Hilgenfeldt (2006). While the recirculation flow is intriguing, it is clearly not directly suitable for MEMS applications, as there is no control over the direction of the flow or the magnitude of the substantial forces experienced by suspended objects such as vesicles or cells (see Marmottant & Hilgenfeldt 2003).

A fortuitous observation recently revealed that the presence of a quartz particle suspended in the liquid near a bubble breaks the symmetry of the vortex flow (see Marmottant & Hilgenfeldt 2004), introducing an element of directionality. In this article, we demonstrate quantitative understanding and application of this effect, establishing bubble-driven microfluidic devices for novel modes of liquid transport and force actuation on suspended objects.

2. Experimental set-up

2.1. *Bubble size control*

To assign the position of the bubbles in experiments, we etch small indentations ('pits') into the hydrophobic substrate. In water, the pits automatically retain air pockets, of size and shape determined by the dissolved gas content of the liquid as follows. The pits are cylinders of depth H and radius R, containing a volume $V_s = \pi R^2 H$ of air below the substrate surface (see figure 1*a*). The interface above the pit takes the shape of a spherical cap of radius a and volume $V_c = V_h(1 \pm \sqrt{1 - (R/a)^2}(1 + R^2/2a^2))$, where $V_h = 2\pi R^3/3$ is the volume of a hemispherical cap. The plus sign is valid if the cap is larger than hemispherical, the minus sign for shallower caps. V_c changes by gas diffusion into or out of the bubble, depending on the saturation concentration c_0 of the gas in the liquid (at ambient pressure p_0) and the concentration c_∞ far from the bubble. Using the quasi-steady limit of the diffusion equation in spherical polar
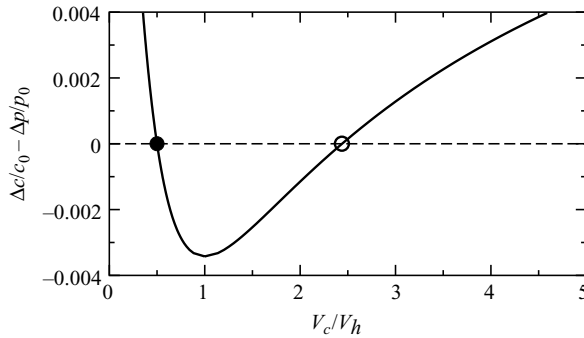
FIGURE 2. The relative supersaturation $[\Delta c/c_0 - \Delta p/p_0] \propto \dot{V}_c$ as a function of relative cap volume V_c/V_h. The solid and open circles mark the stable and unstable equlibrium volumes, respectively.

coordinates (see Brennen 1995; Hilgenfeldt, Lohse & Brenner 1996) for the gas concentration in the liquid, it is easy to show that the rate of bubble volume change is

$$\dot{V}_c = 2\pi Dac_0 \left(1 \pm \left(1 - \frac{R^2}{a^2} \right)^{1/2} \right) \left[\frac{\Delta c}{c_0} - \frac{\Delta p(a)}{p_0} \right], \qquad (2.1)$$

where D is the gas diffusion coefficient, $\Delta c \equiv c_\infty - c_0$ and $\Delta p(a) \equiv 2\gamma/a$ is the Laplace–Young pressure at surface tension γ.

When the water is supersaturated, $\Delta c/c_0 > 0$ and the bubble grows unless a is small enough for $\Delta p(a)$ to counteract the growth. Figure 2 shows the quantity in square brackets in (2.1) as a function of V_c/V_h. If $\Delta p(R)/p_0 > \Delta c/c_0$, two equilibrium points (zeros of $\dot{V}_c$) appear, of which that with the smaller volume is stable. A bubble with a less than hemispherical cap can thus persist indefinitely in a microfluidic flow device.

In experiments, we adjust the bubble size by mixing room-temperature saturated water with a fraction ϕ_s of water that was saturated at refrigerator temperatures (typically 8°C). As the saturation concentration of air in water is about 25 % higher in the cold water, mixing at $\phi_s \approx 0.1$ results in a mixture with supersaturation $\Delta c/c_0 \approx$ 0.025. For air in water ($\gamma \approx 0.07 \, \text{kg s}^{-2}$) and $R \approx 50 \, \mu\text{m}$, this number is just below $\Delta p(R)/p_0$, and we indeed observe stable, almost hemispherical bubble caps whose shape and size does not change for hours.

Larger, more than hemispherical bubbles can also be used in experiments, as long as the time scale over which V_c changes is long compared to the microfluidics time scales. See figure 1(b–e) for a bubble in water of higher supersaturation growing over the course of a few hours.

2.2. *Substrate layout and manufacture*

Instead of the floating particle observed in Marmottant & Hilgenfeldt (2004), whose position cannot be assigned independently, we manufacture small solid protrusions on the substrate ('bumps') close to the pits in order to break the flow symmetry. We manufacture arrays of pits and bumps (which use call 'doublets') (figure 3a) in a silicon master substrate (figure 3b) by reactive ion-etching (see de Boer *et al.* 2002), and replicate the pattern in PDMS (poly-dimethylsiloxane, Dow Corning) see figure 4. The microfluidic flow is observed through an inverted microscope by video-rate or high-speed photography. Images are taken through the bottom wall or through a sidewall of the cuvette. Our doublet arrays feature pits with radii between 15 and 50 μm, combined with cylindrical bumps of $a_{bump} \simeq 60 \, \mu\text{m}$ radius and 30 μm
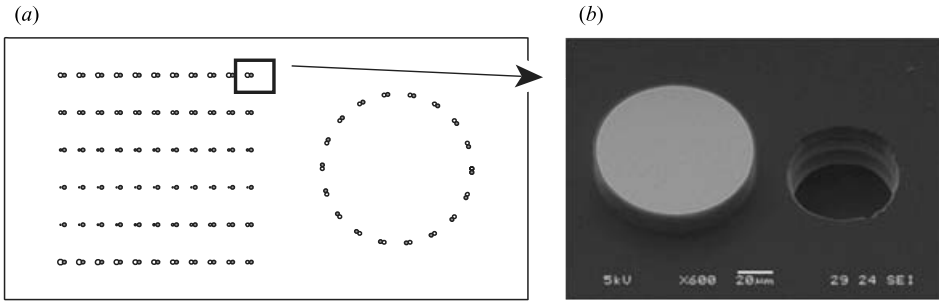
FIGURE 3. (*a*) Substrate design with linear and circular arrays of pit/bump doublets on a substrate of 7×14 mm size. (*b*) Electron micrograph of an etched cylindrical protrusion and adjacent hole in silicon.
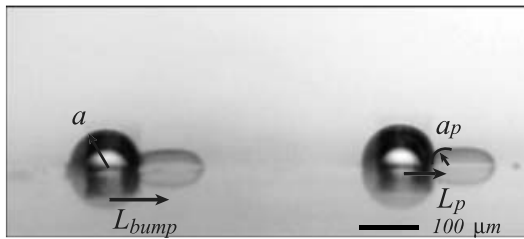

FIGURE 4. Side view after exposing the PDMS substrate to water. Microbubbles have grown in the pits, forming doublets of bubbles and bumps. To model acoustic streaming, bumps are replaced with spheres of effective radius a_p, located at a distance L_p from the bubble. The centres of a bubble and bump are at a height of h_b and h_p above the substrate, respectively.

height. The distance between the centres of a pit and bump within one doublet is $L_{bump} \simeq 95 \,\mu$m, that between successive doublets is $\Delta \simeq 500 \,\mu$m.

The driving ultrasound frequency $f \sim 20$–200 kHz was usually chosen to be resonant with the bubble size. The ultrasound driving amplitude at the location of the bubbles is quite small, resulting in linear bubble oscillations ($\epsilon \lesssim 0.05$, from which we infer ultrasound peak pressures $\lesssim 0.05$ bar via the linearized Rayleigh–Plesset equation (see Brennen 1995). No cavitation was observed anywhere in the cuvette, although vigorous streaming transport flow was induced.

3. Transport

A bump next to a bubble directs liquid towards and beyond this protusion, in the direction of the vector pointing from the bubble towards the bump. Figure 5 shows that fluorescent tracer beads (radius 1 μm) are indeed transported in the streaming flow induced around the bubble/bump combinations. Each doublet in a linear array 'forwards' the beads to the neighbouring doublet downstream.

We find that the trajectories can be relatively direct and unidirectional (figure 5) or more complex, with several bounces off the bubbles (figure 6*a*), even though the doublet geometry (a, L_{bump}, Δ) is the same. We show below how to understand and quantify these flow differences.

By excising single arrays and orienting them randomly, we verified that the cuvette geometry does not bias the transport direction: transport always occurs along the line of doublets. Likewise, the 'storage ring' on the right of the substrate in figure 3(*a*)
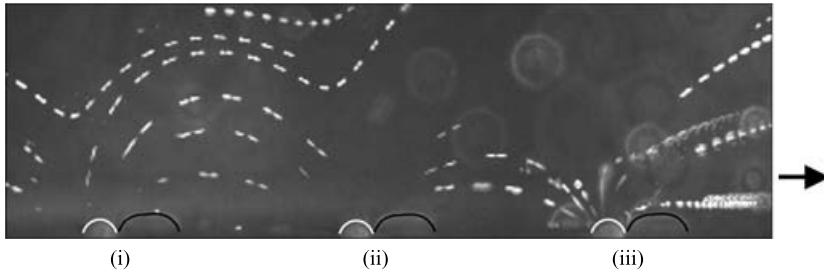
FIGURE 5. Side view of three bubble/bump doublets (i), (ii), (iii) in experiment when bubbles are vibrating in response to ultrasound, with long-time exposure showing the transport of fluorescent beads in the indicated direction (bubble radius $a = 30\,\mu$m). Trajectories in the plane perdicular to the wall are visible.
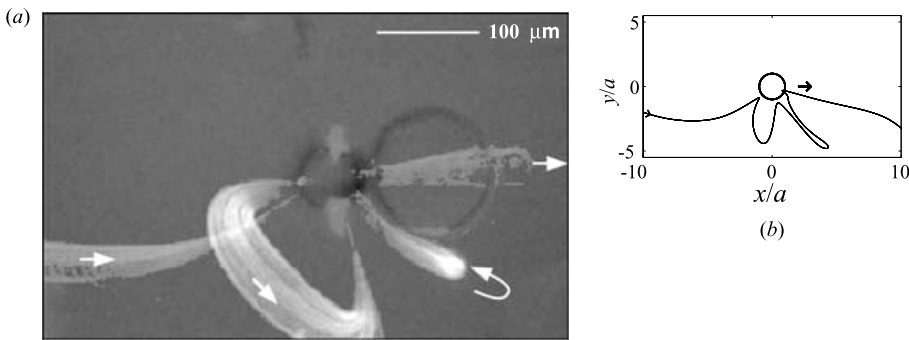

FIGURE 6. (*a*) Top view of a streak image of a fluorescent bead around a single doublet with $a \simeq 30\,\mu$m. The bead streak (arrows) appears the wider the farther it is out of focus, above the substrate plane. (*b*) Trajectory with characteristic bounces reproduced by theory calculations (line). Bubble and bump singularities are positioned at $(0, a)$ and $(2a, a/2)$ in the (x, z)-plane, respectively. Computational parameters are $s = 0.11$ and $\ell_p = 30\,\mu$m.

attracts vesicles from the bulk liquid and transports them along the ring. In all cases, the transport occurs in the direction given by the position of a bubble's closest neighbouring bump.

A recent theory (see Marmottant & Hilgenfeldt 2004) postulated transport flow as the combination of two kinds of acoustic streaming: the steady flow around the oscillating bubble itself, and the steady flow induced by the bubble around another object in the flow. The latter is due to the periodic motion of liquid driven over the object by the oscillating bubble, again resulting in a second-order steady streaming flow. This flow field has been computed analytically when the object is a solid sphere by Amin & Riley (1990) and described using Stokes flow singularity theory (see Blake & Chwang 1974; Marmottant & Hilgenfeldt 2003), which is applicable because the Reynolds number of the steady flow is small (see Lighthill 1978).

The relative amplitude of these two streaming flows can be estimated from the simple scaling arguments developed in the introduction. Around the bubble, the oscillatory amplitude is $u_{1,b} \sim \epsilon a \omega$ and the gradient length scale is $\ell_b = a$, giving a streaming velocity $u_{s,b} \sim u_{1,b}^2/\omega \ell_b \sim \epsilon^2 a \omega$. We now introduce the characteristic streaming velocity $u_s = \epsilon^2 a \omega$. At the position of the solid particle (i.e. the bump), the primary monopole oscillatory flow (decaying as the square of distance) has amplitude $u_{1,p} \sim u_{1,b}(a/L_p)^2$, where L_p is the distance between the centres of a bubble and particle. The streaming
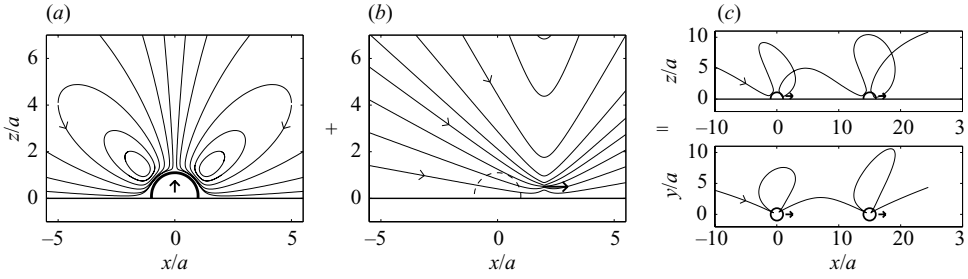
FIGURE 7. (*a*) Side view (x, z-plane) of the steady streaming flow field around a bubble of radius a adsorbed in a pit at a wall, computed from singularity theory. The bubble centre is at $(x_b, h_b) = (0, a/4)$. (*b*) Leading-order flow field of streaming around a solid sphere, modelling the bump, located at $(x_p, h_p) = (2a, a/2)$. (*c*) Adding (*a*) and (*b*) results in doublet streaming trajectories, shown in side and bottom view. Here, $s = 0.05$ and $\Delta/a = 15$ (see text).

flow at the position of the particle then has a magnitude of about $u_{1,b}^2 (a/L_p)^4/(\omega a)$. However, if the exciting bubble is far away ($L_p \rightarrow \infty$), there can be no net transport flow, as the induced flow must be symmetric around the particle. The asymmetry of the streaming flow only appears to first order in a_p/L_p, where a_p is the extent of the bump (here an equivalent spherical radius, see figure 4). Therefore, the order of magnitude of the directional flow speed becomes $u_{s,p} \sim u_{1,b}^2/(a/L_p)^4/(\omega a)a_p/L_p \sim u_s a^4 a_p/L_p^5$, a result which will be made more quantitative below.

The shape of steady flow created by the bubble oscillation by itself is described by a superposition of singularities at the bubble centre, where the leading-order singularity can be described by either a fixed point force or a fixed dipole directed perpendicular to and away from the wall (see figure 7*a*). In the present case the bubble is a portion of a sphere only, and we position the far-field singularity so as to cancel out the flow field at the upper pole of the bubble, in order to comply approximately with the boundary conditions at the bubble wall (for instance the singularity position is $h_b/a \simeq 0.25$ when the bubble centre is on the wall). The streaming flow field around a bubble near a wall can be approximately represented by

$$u_i^{(b)} = u_s \sin(\Delta\phi)\left[\tfrac{1}{2}S_{iz}^W(\mathbf{r}_b/a) - \tfrac{1}{4}M_{iz}^{D,W}(\mathbf{r}_b/a) - \tfrac{1}{2}M_{iz}^{H,W}(\mathbf{r}_b/a)\right], \quad (3.1)$$

where $u_s = \epsilon^2 a\omega$ is the streaming velocity scale of a bubble oscillating with angular frequency ω and amplitude ϵa. $\Delta\phi$ is the phase shift between the radial and translational oscillations of the bubble (Marmottant *et al.* 2006). S_{ij}^W, $M_{ij}^{D,W}$ and $M_{ij}^{H,W}$ are respectively non-dimensional Green's functions of a point force, a dipole (Pozrikidis 1992), and a projection of hexadecapole singularities placed at the bubble centre (Longuet-Higgins 1998), all taking into account the presence of a wall. Coordinates are relative to the bubble centre $\mathbf{x}_b$, introducing $\mathbf{r}_b = \mathbf{x} - \mathbf{x}_b$. For more details and a quantitative derivation of the flow field around a hemispherical bubble attached to a wall see Hansen *et al.* (2006).

For the streaming around a solid sphere, we use the leading-order term from the exact infinite series derived by Amin & Riley (1990), i.e. a point force directed parallel to the wall (arrow in figure 7*b*):

$$u_i^{(p)} = \frac{3}{8}u_s\frac{a_p a^4}{L_p^5}\frac{D^4}{(D^2 - 1)^2}S_{ix}^W(\mathbf{r}_p/a), \quad (3.2)$$

where L_p is the distance between the centres of a bubble and particle and a_p the radius of the solid particle (assumed to be spherical). The distance parameter is $D = L_p/a_p$, and S_{ix}^W is the flow generated by a unit point force parallel to the wall, with coordinates now relative to the particle position, $\boldsymbol{r}_p = \boldsymbol{x} - \boldsymbol{x}_p$. Note that this quantitative result reproduces the dependences on distance and particle size obtained from the estimate above.

The streaming flow around a bubble next to a solid object is the sum of these two low-Reynolds-number flows. In a first approximation we neglect the modifications to both flows resulting from the presence of the other object's boundary. The singularities are sufficiently far apart – the velocity fields decay rapidly with distance – to warrant this simplification. The finite extent of the bump is also neglected, and we therefore expect the modelling to be correct for the far field away from the particle.

The resulting streamlines (see an example in figure 7c) display all the characteristics of the experimental trajectories: a number of bounces off the bubble (reminiscent of the steady recirculation around a single bubble) and a preferred overall transport direction. The prominence of both features depends on the relative strength of the two streaming flows, which we quantify now.

Taking into account prefactors from the rigorous theory for vibrating bubbles and for solid spheres of radius a_p (see equations (3.1) and (3.2)), we find that the relative strength of particle and bubble near-field streaming flows $u_{s,p}/u_{s,b} \equiv s$ is given by

$$s = \frac{3}{8} \frac{a_p a^4}{L_p^5} \frac{D^4}{(D^2 - 1)^2} \frac{2}{\sin(\Delta\phi)} .$$ (3.3)

For larger distances from the doublet, far-field effects become significant, which depend crucially on the standoff distance h_b of the bubble from the wall (see Pozrikidis 1992; Marmottant & Hilgenfeldt 2004). Depending on whether a bubble protrudes more or less from its pit, h_b is larger or smaller. The overall transport flow is therefore characterized by s and a second, independent parameter h_b/a.

The height of the cylindrical bumps used in the experiments varies most strongly near their edge over a length scale comparable with the bump height (figure 4), i.e. the gradient length scale is $\ell_p \simeq 30\,\mu\text{m}$. The streaming around the bump is therefore estimated by replacing it with a sphere of radius $a_p = \ell_p$ located on the bump edge closest to the bubble (where the induced streaming is strongest), at a distance $L_p = L_{bump} - (a_{bump} - \ell_p)$, see figure 4. The doublets in both figures 6(b) and figure 8(a) (the latter highlights one trajectory from figure 5) are thus characterized by the same a_p and L_p, resulting in equal $s \simeq 0.11$. Consistent with the observation that the bubbles protrude more from the pits in figure 6(b) than in figure 8(a), the former is modelled with larger h_b/a, which indeed captures the differences in trajectory shape between the two cases. The agreement is not exact, as the details of doublet flow are sensitive to initial conditions, in particular when the bubble component is dominant, as in figure 6(b). The weaker bubble streaming (because of smaller h_b/a) leads to more effective directional transport with fewer bounces off the bubbles in figure 8, where measured transport velocities exceed $1\,\text{mm}\,\text{s}^{-1}$.

With this theoretical understanding, the direction, speed, and transport strength of the flow can be mastered by changes in substrate patterning and manufacture – a necessary condition for working MEMS devices based on bubble streaming. We now show that the shear forces experienced by objects in the flow can also be controlled and tailored to a range of applications.
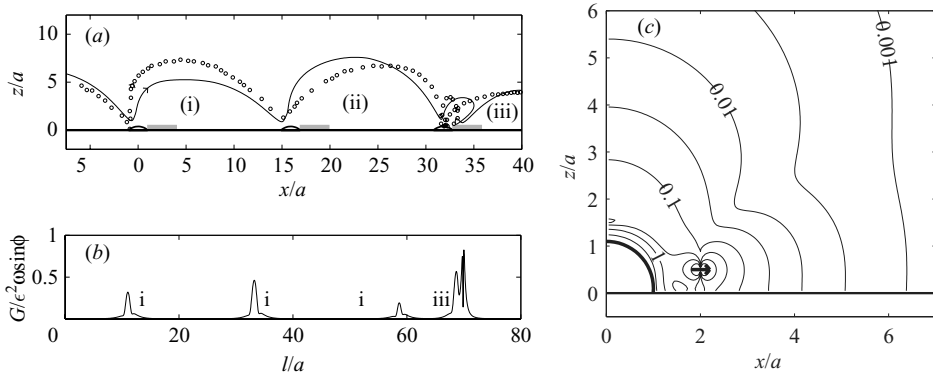
FIGURE 8. (*a*) Transport trajectories of fluorescent particles (side view) through a doublet array, along with trajectories computed from theory reproducing the observed behavior (continuous lines, side view). The experimental parameters were $a \approx 30\,\mu m$, $L_{bump} = 95\,\mu m$, $\Delta = 500\,\mu m$; the computations were performed with $s = 0.11$, $\Delta/a = 16$, $L_p/a = 2$, $h_b/a = 0.5$, $h_p/a = 0.5$. (*b*) Computed Frobenius norm G of the rate-of-strain tensor G_{ij} along the trajectory in (*a*), as a function of distance l. A particle on the trajectory experiences a local maximum of stress at points (i), (ii) (closest approach to the bubble) and (iii) (closest approach to the particle). (*c*) Contour map of G in the (x, z)-plane containing bubble and particle centres.

4. Shear forces

When transported objects abruptly bounce off the doublets, they are exposed to large shear. From the theoretical velocity field u_i, the rate-of-strain tensor $G_{ij} = (\partial_j u_i + \partial_i u_j)/2$ can be evaluated to quantify shear in the flow. Figure 8(*b*) shows that the Frobenius norm $G = \sqrt{G_{ij} G_{ji}}$ has pronounced local maxima at every bounce. The largest strain rate is encountered near the bump, which therefore introduces a well-defined focus for the application of shear stresses on transported objects (see figure 8*c*). Replacing the tracer beads by giant unilamellar lipid vesicles (GUVs, made of di-oleoyl-phosphatidylcholine and manufactured by electroformation (see Marmottant & Hilgenfeldt 2003) with radii between 10 and 100 μm allows direct observation of the effects of the shear. Figure 9 shows that GUVs rupture close to the bump of a doublet, as expected.

In the vortex streaming flow of single bubbles rupture invariably results in complete lysis of the vesicle (see Marmottant & Hilgenfeldt 2003). In a doublet flow with strong enough transport component, however, the vesicle is carried to the region of smaller shear between doublets, where the membrane reseals (figure 9*c*). Some interior vesicle material is expelled. In a device using whole cells, such a process could achieve transfection of drugs or plasmids into the cells (see Miller & Quddus 2000; Shi *et al.* 2002). Only a multiple-doublet set-up with the correct parameters allows this localization of shear stress in space and time, and the transient poration of membranes.

The stress exerted in a liquid of viscosity η on a vesicle of radius R is $\sigma \sim \eta R G$, and the resulting force (on a vesicle circumference) is $F \sim 2\pi R \sigma$. With $G \sim \epsilon^2 \omega$ (cf. figure 8*b*) and experimental values as in figure 9 ($R = 25\,\mu m$, $f = 50\,kHz$, $\eta = 1.3\,cP$, $\epsilon \simeq 0.05$), a vesicle can easily experience $F = 10\,nN$ on a trajectory close to the bump singularity. Even the mechanically toughest cells could thus be probed or porated 'on the fly' in a cytometry or biomedical lab-on-a-chip application. As the velocity scale of the bubble streaming flow is $u_{0,b} = \epsilon^2 a \omega$ and the resonance frequency of a bubble (see Brennen 1995) is proportional to $1/a$, $u_{0,b}$ is independent of bubble size at equal ϵ. Further miniaturization of doublets will therefore allow more efficient devices.
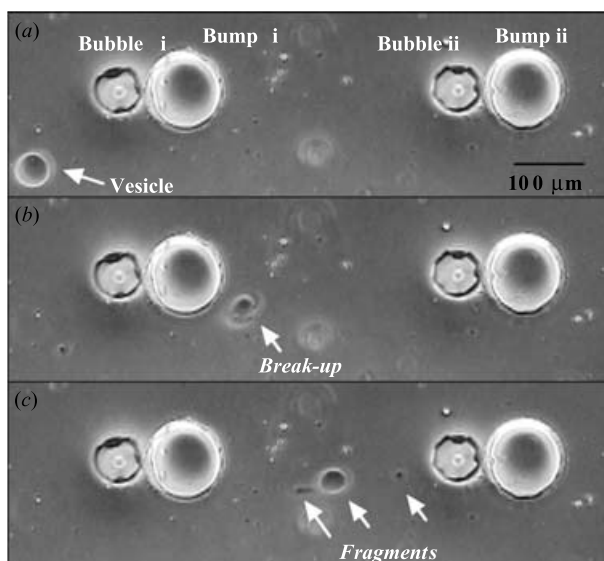
FIGURE 9. Image sequence of vesicle transport between two doublets (very low-amplitude ultrasound is used to slow the process down, ultrasound frequency $f = 48$ kHz). A vesicle of radius $R \simeq 25\,\mu$m is attracted by the first doublet (*a*, time 0 s) and ruptured as it passes the bump (*b*, 0.52 s). When transported towards the following doublet, the membrane reseals (*c*, 0.88 s).

5. Conclusion

Bubble-induced microstreaming flow is very different from previous methods where bubbles have been used as pistons undergoing large volume changes to pump liquid (see Yuan & Prosperetti 1999) or operate valves and switches (see Jackel, Johnson & Tomlinson 1990; Papavasiliou, Pisano & Liepmann 2001). The high efficiency of bubble streaming (see Nyborg 1958) and the directional control distinguish the present method from streaming off vibrated solids (see Lutz, Chen & Schwartz 2003). The low driving amplitudes of ultrasound avoid any substantial heating of the working fluid, in contrast to streaming induced in the bulk of the liquid via the dissipative 'quartz wind' effect (see Lighthill 1978). Microfluidic transport is accomplished here without pressure gradients and without microchannels, eliminating precautions against clogging of channels in two-phase applications. The thorough understanding of the process through Stokes singularity theory allows direct design of microfluidic MEMS for transport, storage, guidance, and other tasks: the substrates presented here were designed on the computer and performed just as predicted. As each bubble on the substrate is a micron-scale actuator driven by the cm-scale ultrasonic field, a large number of bubble devices can be driven simultaneously. This enables a high degree of parallelization and microfluidics with high throughput.

REFERENCES

AMIN, N. & RILEY, N. 1990 Streaming from a sphere due to a pulsating source. *J. Fluid Mech.* **210**, 459–473.

BEEBE, D. J., MOORE, J. S., BAUER, J. *et al.* 2000 Functional hydrogel structures for autonomous flow control inside microfluidic channels. *Nature* **404**, 588–590.

BLAKE, J. R. & CHWANG, A. T. 1974 Fundamental singularities of viscous flow. *J. Engng Maths* **8**, 23–29.

DE BOER, M. J., GARDENIERS, J. G. E., JANSEN, H. V. *et al.* 2002 Guidelines for etching silicon mems structures using fluorine high-density plasmas at cryogenic temperatures. *J. Micromech. Syst.* **11**, 385–401.

BRENNEN, C. E. 1995 *Cavitation and Bubble Dynamics*. Oxford University Press.

HANSEN, D., MARMOTTANT, P. & HILGENFELDT, S. 2006 Steady streaming from surface-adsorbed microbubbles. Submitted.

HILGENFELDT, S., LOHSE, D. & BRENNER, M. P. 1996 Phase diagrams for sonoluminescing bubbles. *Phys. Fluids* **8**, 2808–2826.

JACKEL, J. L., JOHNSON, J. J. & TOMLINSON, W. J. 1990 Bistable optical switching using electrochemically generated bubbles. *Opt. Lett.* **15**, 1470–1472.

KOPP, M. U., DE MELLO, A. J. & MANZ, A. 1998 Chemical amplification: continuous-flow PCR on a chip. *Science* **280**, 1046–1048.

LIGHTHILL, J. 1978 Acoustic streaming. *J. Sound Vib.* **61**, 391–418.

LONGUET-HIGGINS, M. S. 1998 Viscous streaming from an oscillating spherical bubble. *Proc. R. Soc. Lond.* A **454**, 725–742.

LUTZ, B. R., CHEN, J. & SCHWARTZ, D. T. 2003 Microfluidics without microfabrication. *Proc. Natl Acad. Sci.* **100**, 4395–4398.

MARMOTTANT, P. & HILGENFELDT, S. 2003 Microacoustics: Controlled vesicle deformation and lysis by single oscillating bubbles. *Nature* **423**, 153–156.

MARMOTTANT, P. & HILGENFELDT, S. 2004 A bubble-driven microfluidic transport element for bioengineering. *Proc. Natl Acad. Sci.* **101**, 9523–9527.

MARMOTTANT, P., VERSLUIS, M., DE JONG, N., HILGENFELDT, S. & LOHSE, D. 2006 High-speed imaging of an ultrasound-driven bubble in contact with a wall: 'Narcissus' effect and resolved acoustic streaming. *Exps. Fluids* **41**, 147–153.

MILLER, D. L. & QUDDUS, J. 2000 Sonoporation of monolayer cells by diagnostic ultrasound activation of contrast-agent gas bodies. *Ultrasound Med. Biol.* **26**, 661–667.

NYBORG, W. L. 1958 Acoustic streaming near a boundary. *J. Acoust. Soc. Am.* **30**, 329–339.

PAPAVASILIOU, A., PISANO, A. P. & LIEPMANN, D. 2001 High-speed and bi-stable electrolysis-bubble actuated gate valves. In *Proc. 11th Intl Conf. on Solid State Sensors and Actuators (Transducers '01)*, pp. 940–943. Munich, Germany.

POZRIKIDIS, C. 1992 *Boundary Integral and Singularity Methods for Linearized Viscous Flow*. Cambridge University Press.

SHI, X., MARTIN, R. W., VAEZY, S. & CRUM, L. A. 2002 Quantitative investigation of acoustic streaming in blood. *J. Acoust. Soc. Am.* **111**, 1110–1121.

SOLOMON, T. H. & MEZIĆ, I. 2003 Uniform resonant chaotic mixing in fluid flows. *Nature* **425**, 376–380.

SQUIRES, T. M. & QUAKE, S. R. 2005 Microfluidics: Fluid physics at the nanoliter scale. *Rev. Mod. Phys.* **77**, 977.

STONE, H. & KIM, S. 2001 Microfluidics: Basic issues, applications, and challenges. *AIChE J.* **47**, 1250–1254.

STROOCK, A. D., DERTINGER, S. K. W., ADJARI, A., MEZIĆ, I., STONE, H. & WHITESIDES, G. M. 2002 Chaotic mixer for microchannels. *Science* **295**, 647–651.

THORSEN, T., MAERKL, S. J. & QUAKE, S. R. 2002 Microfluidic large scale integration. *Science* **298**, 580–584.

YUAN, H. & PROSPERETTI, A. 1999 The pumping effect of growing and collapsing bubbles in a tube. *J. Micromech. Microengng* **9**, 402–413.